
Transfer learning for atomistic simulations using GNNs and kernel mean embeddings

John Falk
CSML

Istituto Italiano di Tecnologia
Genova, Italy
me@isakfalk.com

Luigi Bonati

Atomistic Simulations

Istituto Italiano di Tecnologia
Genova, Italy
luigi.bonati@iit.it

Pietro Novelli

CSML

Istituto Italiano di Tecnologia
Genova, Italy
pietro.novelli@iit.it

Michele Parrinello

Atomistic Simulations

Istituto Italiano di Tecnologia
Genova, Italy
michele.parrinello@iit.it

Massimiliano Pontil

CSML

Istituto Italiano di Tecnologia
Genova, Italy
and

Department of Computer Science
University College London, UK
massimiliano.pontil@iit.it

Abstract

Interatomic potentials learned using machine learning methods have been successfully applied to atomistic simulations. However, deep learning pipelines are notoriously data-hungry, while generating reference calculations is computationally demanding. To overcome this difficulty, we propose a transfer learning algorithm that leverages the ability of graph neural networks (GNNs) in describing chemical environments, together with kernel mean embeddings. We extract a feature map from GNNs pre-trained on the OC20 dataset and use it to learn the potential energy surface from system-specific datasets of catalytic processes. Our method is further enhanced by a flexible kernel function that incorporates chemical species information, resulting in improved performance and interpretability. We test our approach on a series of realistic datasets of increasing complexity, showing excellent generalization and transferability performance, and improving on methods that rely on GNNs or ridge regression alone, as well as similar fine-tuning approaches. We make the code available to the community at https://github.com/IsakFalk/atomistic_transfer_mekrrr.

1 Introduction

Atomistic simulations have become a pillar of modern science and are pervasively used in many areas of physics, chemistry, and biology. Among these techniques, molecular dynamics plays a prominent role. This method simulates the time evolution of a system of atoms by integrating Newton's equation of motion [1]. The forces acting on the atoms are determined from a model for the interactions, called the potential energy surface (PES), on whose accuracy the reliability of the simulation depends. For a long time, the interactions were modeled in a rather empirical, and of course, not very accurate way [1, 2]. A major step forward was made with the introduction of *ab initio* molecular dynamics in which the interactions are computed on the fly from accurate electronic structure calculations [3, 4]. This implies solving at every step the Schroedinger equation, typically with the use of some approximation such as the popular Density Functional Theory (DFT) scheme [5].

This approach is much more accurate but at the same time more computationally expensive, limiting the system size (i.e. the number of atoms) and time scale which can be simulated.

Starting with the work of Behler and Parrinello [6], machine learning potentials have emerged as promising candidates to alleviate the tension between accuracy and efficiency [7, 8]. They regress the potential energy, as a function of the atomic positions and the chemical species, on a (large) set of expensive *ab initio* calculations. Once successful, this strategy results in a model of the potential energy that has an accuracy close to *ab initio* one at a fraction of the cost, typically speeding up simulations by orders of magnitude. Several machine learning approaches have been successfully used in this context, see e.g. [7] and references therein. Particularly relevant for this paper are those based on kernel ridge regression (KRR) [9–11] as well as graph neural networks (GNNs) [12–16].

Modeling the potential energy is complicated by the need to impose important physical symmetries like translational, rotational, and permutational invariance [7]. Furthermore, one needs to ensure that energy is an extensive quantity. While learning these symmetries can be encoded in the architecture of the network [15–17], this comes at a sizeable computational cost. On the other hand, the manual selection of invariant physical descriptors [6, 18–20] is a complex procedure that limits the application to systems characterized by many chemical species.

In this paper, we take a different approach and exploit the availability of large datasets to model the potential energy in a more accurate but also efficient way. We rely on the Open Catalyst dataset [21], created having in mind heterogeneous catalysis applications, which contains $\sim 250\text{M}$ DFT calculations obtained from relaxations of molecules adsorbed on surfaces. Our approach mirrors other developments in machine learning [22–27] where the use of large datasets has led to advances in terms of modeling and transfer capabilities of the so-called foundation models [28].

Contributions This paper makes the following contributions:

- We propose a transfer learning algorithm, mean embedding kernel ridge regression (MEKRR), for modeling the potential energy surface of atomic systems which combines GNN representations pre-trained on large datasets with kernel mean embeddings.
- We introduce a new kernel function in the context of modeling potential energy surfaces, which exploits chemical species information. This shows superior performance and facilitates monitoring the chemical evolution of the system.
- Our method shows excellent generalization and transferability performance. This is demonstrated through a series of experiments of increasing complexity derived from molecular dynamics simulations of catalytic processes, including chemical reactions that are not present in the pre-training dataset.

Related work This work builds upon two main directions; representation and transfer-learning, and kernel methods for learning potential energy surfaces. In terms of transfer learning, we take inspiration and build upon a long line of work on transferring deep representations on images and the surprising effectiveness of traditional regression and classification models on top of pre-trained feature maps. All of [29–33] use pre-training in the context of meta-learning and then use a simple algorithm at test time to transfer. In particular, our method is similar to [33] which employ KRR on top of a meta-learned feature map but they do not focus on instances that are sets. Pre-training strategies in the context of modeling the potential energy surface of extensive systems are scarce due to difficulty in generating large datasets, and just started to appear [34] following the release of the Open Catalyst dataset [21].

For methods based on kernels for modeling the potential energy, we are similar in spirit to [9, 18] but instead of representing the environment of the atoms in terms of handcrafted radial and harmonic expansion terms we use a pre-trained GNN to represent each system as a point cloud given by the GNN representation. Similarly [10, 35, 36] use KRR but by construction cannot transfer beyond one system. [37] outlines a way to incorporate automatic differentiation to speed up fitting gradients in KRR and experiment with composing GNNs with traditional kernels but again cannot transfer across systems.

Organization In Section 2 we specify the problem we are aiming to solve, with Section 2.1 and Section 2.2 setting up the machine learning problem. In Section 3 we introduce the kernel mean embedding framework together with KRR and in Section 4 we introduce our method MEKRR. In

Section 5 we validate our method on a variety of realistic datasets of increasing complexity. Finally, in Section 6 we conclude and outline future directions.

2 Learning PES from atomistic simulations

In this section, we introduce the setting and the objectives related to modeling the PES from atomistic data.

2.1 Setting

We consider systems composed of n atoms and S different chemical species, described via one-hot-encoding over $[S]$, where $[S] = \{1, \dots, S\}$. Each atom is described by its Euclidean position $r \in \mathbb{R}^3$ and its chemical species $z \in \{0, 1\}^S$. We denote a state of the system by $x = (r_i, z_i)_{i=1}^n = (R, Z) \in \mathcal{X}$ using the design matrices $R \in \mathbb{R}^{n \times 3}$ and $Z \in \{0, 1\}^{n \times S}$.

The quantity we want to regress is the potential energy, which is a scalar function $E : \mathcal{X} \rightarrow \mathbb{R}$. The target values E_t are calculated by querying the *ab initio* method of choice, which we refer to as the oracle. By means of molecular dynamics simulations, one can obtain a sequence of T configurations $(x_t)_{t=1}^T$ which compose the datasets together with their corresponding labels $D = (x_t, E_t)_{t=1}^T$.

The physics of the system posits that any estimator of the energy $\hat{f} : \mathcal{X} \rightarrow \mathbb{R}$ should possess certain invariant properties reflecting the underlying physical symmetries. These invariances are *roto-translational invariance* with respect to the position vectors and *permutation-invariance within each group of chemical species*. In addition, the estimator of the energy should be curl-free and smooth [12]. A wealth of previous works introduced deep learning architectures incorporating these invariances by design [e.g. 12, 14, 15, 38]. Our transfer-learning scheme works by exploiting these invariant architectures so that the final fine-tuned estimator is invariant as well.

2.2 Objective function

We consider an energy estimator $\hat{f} = f_w$ from a set of functions (e.g. a reproducing kernel Hilbert space or neural network functions) parameterized by w , which we want to optimize on a given dataset D . This is achieved by minimizing an objective function, which can be split into a data-fitting term and a regularizer which encourages functions of low complexity.

Typically, the data fitting term is a least squares loss, a sum over point-wise losses between an output y and prediction \hat{y} , $\ell(y, \hat{y})$. In the case of a scalar output such as the energy this amounts to $\ell(E, \hat{E}) = (E - \hat{E})^2$, while for vector outputs to $\ell(y, \hat{y}) = \|y - \hat{y}\|^2$, where $\|\cdot\|$ is the Euclidean norm. The latter case is used when fitting additional information such as the forces, which are defined as $F(x, r) = -\nabla_r E(x)$, the negative Jacobian of E evaluated at x with respect to r .

In this more general case, the regularized empirical risk minimization objective takes the form

$$\hat{\mathcal{R}}(w) = \sum_{t=1}^T \left(\gamma(E_t - f_w(R_t, Z_t))^2 + (1 - \gamma) \|F_t + \nabla_{R_t} f_w(R_t, Z_t)\|^2 \right) + \lambda \Omega(w), \quad (1)$$

for some regularizer Ω and regularization parameter $\lambda > 0$ and a loss weight $\gamma \in [0, 1]$. Typically we will use $\Omega(w) = \|w\|^2$ as the regularizer, but in Section 4.1 we extend this to incorporate additional information. Since in the experiments discussed below we focus on energy prediction, we let $\gamma = 1$.

3 Reproducing kernels and kernel ridge regression

In this section we introduce reproducing kernel Hilbert spaces (RKHS), kernel mean (or set) embeddings, and kernel ridge regression (KRR). These techniques will be the backbone of our method in Section 4, alongside the pre-trained GNN features. Note that we will not concern ourselves about technicalities of existence and well-definedness, implicitly assuming regularity as is necessary.

Reproducing kernels are a well-established field in machine learning, as they are at the heart of most non-parametric algorithms, see [39] and references therein. Note that the $x \in \mathcal{X}$ below is arbitrary

and not to be confused with our x representing a configuration. Kernels consist of positive (semi) definite functions $K : \mathcal{X} \times \mathcal{X} \rightarrow \mathbb{R}$ on some input space \mathcal{X} , and may be interpreted as encoding similarity between pairs of data points.

Every kernel K and corresponding RKHS \mathcal{H}_K can be shown to be defined through the canonical feature map $\phi_K : \mathcal{X} \rightarrow \mathcal{H}_K$, defined through $\phi_K(x) = K(x, \cdot)$. Reversely, any feature map $\phi : \mathcal{X} \rightarrow \mathcal{H}$ mapping to a Hilbert space \mathcal{H} with inner product $\langle \cdot, \cdot \rangle$ defines a reproducing kernel through $K_\phi(x, x') = \langle \phi(x), \phi(x') \rangle$. One of the key benefits of kernels is that they allow us to express estimators as linear functions $f(x) = \langle f, \phi(x) \rangle$, leading to kernelized algorithms expressed completely through the Gramian matrix of inner products between the input points of some dataset D , which we will show below for the case of KRR (see e.g. [39]) and that our setting is a special case of KRR when we map sets of points to elements in some RKHS using set embeddings.

Kernels are typically used on vectorial inputs but can be readily applied to other types of data, in particular to sets of points such as our configurations x . We assume that we have described the environment of each atom by some feature vector h so that x becomes the set $H = (h_i)_{i=1}^n$. The standard way to define a kernel on a set like H is to use a pointwise kernel k and the corresponding feature map ϕ to define the feature map $\phi(H) = C \sum_{i=1}^n \phi(h_i)$ mapping to \mathcal{H}_k , see [40] and references therein. In essence, we have used a kernel k on points to define a kernel on sets $K(H, H') = \langle \phi(H), \phi(H') \rangle$. The choice of C is important in practice for energy prediction and predicting chemical quantities in general as letting $C = 1/n$ respects intensive quantities while $C = 1$ respects extensive properties (such as the potential energy) when we use a linear model in $\phi(H)$ as shown below. Note that the constant C is dependent on H in general. For $H = (h_i)_{i=1}^n$ and $H' = (h'_j)_{j=1}^{n'}$ the kernel $K(H, H')$ can be expressed as

$$K(H, H') = C_H C_{H'} \sum_{i,j}^{n,n'} k(h_i, h'_j) = C_H C_{H'} \mathbf{1}_n^\top k(H, H') \mathbf{1}_{n'}, \quad (2)$$

where C_H is the constant depending on H , $k(H, H') = (k(h_i, h'_j))_{i,j}^{n,n'}$ is the cross-kernel matrix and $\mathbf{1}_n$ is the vector of ones of size n .

Let $D = (H_t, E_t)_{t=1}^T$ where $H_t = (h(x_t)_i)_{i=1}^n$ is the preprocessed configuration of x_t which is now a set, and assume that we have chosen some kernel k on vectors and in extension K . KRR is the kernelized version of Ridge Regression [41] and in our case can be seen as performing Tikhonov regularization on the least squares loss function over the hypothesis space being an RKHS with kernel K . Standard KRR is the algorithm which solves the problem

$$\hat{w} = \operatorname{argmin}_{w \in \mathcal{H}} \left\{ \sum_{t=1}^T (\langle w, \phi(H_t) \rangle - E_t)^2 + \lambda \|w\|^2 \right\} \text{ with } \langle \hat{w}, \phi(H) \rangle = \sum_{t=1}^T c_t K(H_t, H), \quad (3)$$

where $c = (c_t)_{t=1}^T = (G + \lambda I)^{-1} E$ are the solution coefficients, $G = (K(H_t, H_l))_{t,l}^T$ is the $T \times T$ kernel Gramian matrix, I is the $T \times T$ identity matrix, and $E = (E_1, \dots, E_T)^\top$; see e.g. [39]. In the case that we have the forces it is possible to extend KRR to the vector output case and solve (1) when $\Omega(w) = \|w\|^2$ which reduces to solving a similar linear system as is done with c [37, 42], we will not pursue this direction in this work.

4 Method

Our method relies on the power of set embeddings using a Gaussian kernel in order to do kernel ridge regression. As noted above in Section 3, in order to leverage the kernel K we need to reduce a configuration x to a set H which describes the environment of each atom. To do this, we note the success of foundation models [28] to enable transfer from big datasets to novel settings and which we in practice do by leveraging the pre-trained feature maps on OC20 dataset [21], opting to use the SchNet [12] pre-trained weights.

SchNet is an instance of a graph neural network (GNN) [43] which is a type of neural network which operates on graphs and maps to some output space. A graph $\mathcal{G} = (\mathcal{V}, \mathcal{E})$ is a collection of n nodes \mathcal{V} and edges $\mathcal{E} \subseteq \mathcal{V} \times \mathcal{V}$, between pairs of nodes, together with node feature vectors $H_0 = (h_{0,i})_{i=1}^n$, where we index the nodes in \mathcal{V} by $[n]$. Each edge has an associated weight and the graph may be

completely represented using the node features and the nodes, edges and edge weights. For a node i we let $\mathcal{N}(i)$ be the set of nodes connected to i through an edge, which we call the neighborhood of i . A GNN, and SchNet in particular, is built by stacking GNN layers as follows; for a configuration x we have a preprocessing step which turns x into a graph using the distance matrix of all the atoms and the i 'th atom is associated with the i 'th node in the resulting graph. The i 'th atom is mapped to an initial node feature $h_{0,i} = a_{z_i}$ through a lookup table which may be learned. A layer updates the current node-features $(h_i)_{i=1}^n$ to the next layer features $(g(h_i + \sum_{j \in \mathcal{N}(i)} \eta(h_i, h_j)))_{i=1}^n$ via message passing where g is some non-linear function such as an MLP and η is some message-passing function. The outputs of the final layer are pooled to yield a prediction. The weights of the lookup table and layers are learned in an end-to-end fashion typically using first-order optimization. While there are many GNN architectures [44] we consider explicitly GNNs developed for computational chemistry [e.g. 13–15, 38, 45–49], which could be used in place of SchNet in our implementation.

For a pre-trained GNN, we use some intermediate layer output of depth L to extract H from x . This gives us a pre-trained node-feature map $x \mapsto H$, which we will write as $H = H(x)$, representing chemical environments. We note that due to the initial GNN layer which embeds the i 'th atom to a_{z_i} the feature vector h_i implicitly takes into account the chemical species of atom i and aggregates information in a neighborhood of size L . For the initial embedding a_{z_i} to exist we assume that we only encounter configurations with chemical species which the GNN has encountered during training. By replacing the configurations in the train set with the corresponding node-features H we can perform kernel ridge regression using (3).

4.1 Multi-weight KRR

Above we have considered the setting where the estimator is of the form $f_w(x) = \langle w, \phi(H(x)) \rangle$. To ease notation we work with H directly considering $f_w(H) = \langle w, \phi(H) \rangle$. In our setting we have additional information in terms of the chemical species of each atom. This information is implicitly used by the GNN through the lookup-table embedding layer which embeds each atom of the same chemical species to the same dense feature vector. For a configuration x let $H_s = (h_i | z_i = s)$ be the set of feature maps of atoms of the s 'th chemical species. We consider a multi-weight regression extension of (3) where each set of feature maps of chemical species are given their own weight, while encouraging the weights to be close to each other and of small magnitude through a regularizer. Precisely, let $V = (v_s)_{s=1}^S$ be the set of perturbations of a center weight w_0 for each chemical species. The weight of a chemical species s is given by $v_s + w_0$ and the energy function takes the form $f_{w_0, V}(H) = \sum_{s=1}^S \langle v_s + w_0, \phi(H_s) \rangle$. The regularized objective is reminiscent of the KRR objective, but with a special regularizer that allows interpolating between two different regimes; one where we learn a common weight for each species and one where we learn each species-specific weight without a common mean w_0 . The multi-weight KRR objective is defined to be

$$\sum_{t=1}^T \left(E_t - \sum_{s=1}^S \langle v_s + w_0, \phi(H_{t,s}) \rangle \right)^2 + \lambda \left(\frac{1}{\alpha} \sum_{s=1}^S \|v_s\|^2 + \frac{1}{1-\alpha} \|w_0\|^2 \right), \quad (4)$$

where $\alpha \in [0, 1]$ and with $1/\infty$ interpreted as 0. See Appendix A for a complete derivation. The second (regularization) term in (4) is similar to regularizer used in the different setting of multi-task learning [50, 51], in which multiple tasks are learned jointly. However here the weights also interact together in the first (loss) term of the objective.

The objective (4) may be rewritten in the standard KRR form with kernel

$$K_\alpha(H, H') = (1 - \alpha)K(H, H') + \alpha \sum_{s=1}^S K(H_s, H'_s). \quad (5)$$

The above kernel, which we simply call K_α is a direct generalization of the standard set embedding kernel where the parameter α allows to interpolate between the two kernels $K(H, H')$ and $\sum_{s=1}^S K(H_s, H'_s)$ which emphasize all atomic interactions equally and only within-species atomic interactions, respectively. The multi-weight objective (4) (or equivalently, multi-weight kernel (5)) depends on the hyperparameter $\alpha \in [0, 1]$ which allows us to interpolate between the two settings of standard weight KRR and hard multi-weight KRR. While this enforcement is non-linear in weight space due to how we parameterize the regularizer, it allows us to view the interpolation to be linear when considering K_α .

Algorithm To summarize, given a train set $D = (x_t, E_t)_{t=1}^T$, a pointwise kernel k , interpolation parameter α , KRR regularization parameter λ and a feature map in the form of the output of an intermediate layer of a pre-trained GNN, our method is trained as follows:

1. Create $(H_t)_{t=1}^T$ mapping all configuration through the feature map, store this set of matrices.
2. Form the kernel matrix $G = (K_\alpha(H_t, H_l))_{t,l}^T$ using (2) and (5).
3. Compute KRR coefficients $c = (G + \lambda I)^{-1} E$ where $E = (E_1, \dots, E_T)^\top$.

Then, to predict the energy of a new configuration x , we perform the following steps:

1. Map $x \mapsto H$.
2. Form the vector $v = (K_\alpha(H, H_t))_{t=1}^T$ using the saved matrices from training and (2) and (5).
3. Predict $\hat{E}(x) = c^\top v$ using the KRR coefficients.

5 Experiments

In this section, we consider the realistic problem of modeling the potential energy surface of catalytic reactions occurring on metallic surfaces. We evaluate our approach against methods that are representative of the KRR and GNN approaches, testing them on datasets of increasing complexity. As is customary in the literature, we employ the root mean squared error (RMSE) and mean absolute error (MAE), normalized by the number of atoms, as metrics to facilitate comparisons between systems of different sizes.

5.1 MEKRR and baselines

The baselines lie on two axes, with the first axis deciding if the algorithm falls into the camp of GNNs or kernel methods with handcrafted features. The second axis describes if the method is trained from scratch or relies on transfer learning of some kind. The following are supervised learning algorithms that are trained from scratch on the provided datasets:

SchNet [52] One of the first GNNs to be applied successfully to chemistry. We rely on the code base of [21].

GAP-SOAP Gaussian Process regression framework [9] using Smooth Overlap of Atomic Positions descriptors [53]. We rely on the QUIP code base using the quippy python interface [54, 55].

The following baselines perform some sort of transfer learning for which we rely on the OC20 dataset [21] as a source, by leveraging the provided pre-trained weights:

SchNet-FT Fine-tuning the last few layers of a pre-trained SchNet architecture.

Finally, we consider two variants of our method:

MEKRR Using the pre-trained SchNet GNN as a node embedding feature map which we use in our method with k being a Gaussian kernel with lengthscale fit using the median heuristic [56].

MEKRR- α Same as MEKRR but where we embed all node features according to their chemical species and solve the regression problem using multiple weights, one for each species, as outlined in Section 4.1. The value of α is chosen via cross-validation on a representative of the family of datasets. Note that this corresponds to MEKRR when $\alpha = 0$.

5.2 Datasets

We first describe the dataset which has been used for the construction of the pre-trained GNN feature map, and then present the system-specific MD datasets where our method is fine-tuned on.

OC20 The Open Catalyst (OC) 20 is a large dataset of *ab initio* calculations aimed at estimating adsorption energies on catalytic surfaces. It comprises ~ 250 millions of DFT calculations, generated from over 1.2 million relaxations trajectories of different combinations

of molecules and surfaces. In each relaxation, the positions of the molecule and of the surface upper layers are optimized via gradient descent in order to compute the adsorption energy. The adsorbate is selected out of 82 molecules relevant to environmental applications, while, for each of them, up to 55^3 surfaces are selected, including also binary and ternary compounds. We underline that, for each adsorbate-surface pair, the configurational space sampled is very limited, and especially it does not cover out-of-equilibrium and reactive (e.g. bond forming or breaking) events.

We fine-tune the method and test it on two datasets that are representative of reactive catalytic events, studied by *ab initio* molecular dynamics simulations. Whereas the OC20 dataset contains short, correlated relaxations toward the nearest equilibrium state, typical catalytic reaction datasets require sampling all local minima (adsorption states of the molecule) and especially reactive events, in which, due to interaction with the surface, bonds can be broken or even formed. For this reason, these applications are challenging as they relate to realistic datasets containing mostly reactive events that are outside the distribution of the OC20 dataset. We split all the below datasets into a train, validation and test set using random splitting of 60/20/20.

Cu/formate The first dataset is a collection of molecular dynamics simulations of the dehydrogenation reaction of formate on a copper (Cu) $\langle 110 \rangle$ surface [16], in which the molecule loses its hydrogen atom upon interaction with the surface.

Fe/N₂ (D_i) The second dataset consists of molecular dynamics simulations of a nitrogen molecule adsorbing on a iron (Fe) $\langle 111 \rangle$ surface at high temperature ($T = 700$ K) and breaking in two nitrogen atoms [57]. A peculiarity of this dataset is that it contains data from different sources (e.g. standard and biased molecular dynamics) and system sizes, allowing us to also assess the transferability of the methods across different conditions. For this reason, we divide it into 4 subsets, denoted with D_i :

D_1 : **AI-MD** Ab-initio molecular dynamics simulations. The resulting configurations are highly correlated and cover a small portion of the configurational space related to the adsorption process, thus being the closest dataset to the OC20 one.

D_2 : **AI-METAD** Here the *ab initio* MD simulation is accelerated with the help of the metadynamics [58] technique. This is an importance sampling method that allows rare events to be observed, and thus it has been employed for collecting reactive configurations in the training set [59]. Due to the metadynamics approach, a larger region of configurational space is sampled with respect to D_1 , allowing to sample one bond-breaking event.

D_3 : **AL-METAD** Dataset built from an active learning procedure using an ensemble of NNs combined with metadynamics. In this simulation, multiple reaction events are observed, covering a wider region of the configurational space and providing a large number of uncorrelated samples. Hence, these configurations are far from those used to pre-train the feature map.

D_4 : **AL-METAD-72** Same as D_3 but the surface is composed of 72 atoms (8 layers) to test the transferability across systems of different sizes.

5.3 Interpolating between shared and independent weights

The α parameter in the K_α kernel can vary in the range $[0, 1]$, which are the limiting cases between a shared or independent set of weights for each chemical species. We use cross-validation to set this parameter in practice. To initially fit the regularization parameter λ we set $\alpha = 0$ and cross-validate $\lambda \in \{10^{-3}, \dots, 10^{-9}\}$ using the same datasets. Despite this simple heuristic cross-validation scheme, as we will see, the scheme is effective, which we believe is a strength as it shows that the MEKRR method is simple to tune while still having the strongest performance among the competitors.

In Fig. 1 we show the cross-validation curves related to the two datasets Cu/formate and Fe/N₂ (D_2). The two plots show different behavior with the optimal α for the Cu/formate dataset occurring around 10^{-2} . This means that the potential energy can be well described with shared weights across chemical species together with a small perturbation. Instead, in the Fe/N₂ dataset the optimal α occurs at the boundary leading to a kernel in which the weights for the two species are learned independently.

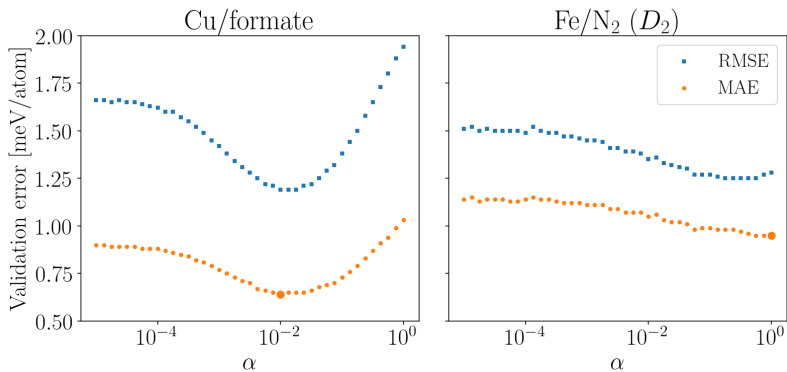


Figure 1: Validation error (RMSE / MAE) of MEKRR- α on the Cu/formate and Fe/N₂ (D_2) datasets as a function of α geometrically spaced on a grid from 0 to 1 with optimal α and error given by a bold orange point. The optimal α for the Cu/formate dataset is positive but close to zero while the optimal α for the Fe/N₂ is found at the boundary at 1.0 leading to a hard multi-weight kernel. We see that tuning the α allows for improved performance in practice and that the multi-weight formulation (4) is practically beneficial.

5.4 Potential energy regression

In this section, we consider the setting of predicting the potential energy surface. We first evaluate the performance of the models in predicting the energy for each of the datasets and then assess their generalization performance through the transfer learning setting, where we train and test on similar but distinct datasets.

Same-dataset energy prediction From Table 1 we see that MEKRR/MEKRR- α performs the best across all datasets, with SchNet-FT tying for best only on D_1 . We note that in general the transfer learning algorithms (SchNet-FT and MEKRR) outperforms the ones trained from scratch. Furthermore, it is worth highlighting that our method performs consistently better with respect to other methods, even when it is applied to datasets that are very different from the OC20 dataset, on which the feature map was pre-trained. This is particularly evident for the datasets D_3 and D_4 which contain multiple reactive (bond breaking) events that were never seen in the relaxations composing the OC20 dataset.

Across-dataset energy prediction In Table 2 we evaluate the performance of the algorithms and α -MEKRR on transferring from different systems in the Fe/N₂ family of datasets. To do this we consider the task of zero-shot transfer learning (see e.g. [60] and references therein) where we evaluate a model trained on a source dataset D_{source} on a target dataset D_{target} . While the two datasets D_{source} and D_{target} may be sampled from arbitrary systems, we consider here systems that share some characteristics as we are evaluating the transfer capability of the models [61, 62]. Due to the ordering of the datasets D_1, \dots, D_4 in increasing complexity on several axes (size, ab-initio vs. active sampling, standard vs. biased dynamics etc.) we consider transfer from simpler to more complicated systems. Successfully transferring from simpler to more complicated systems has real-world impact as it can alleviate the high computational cost required for the labeling via DFT calculations by reducing the number of points. From Table 2 we see that MEKRR clearly gets the best performance, followed by SchNet-FT and SchNet. In this case, we only report the results for MEKRR as cross-validation reports the lowest error for $\alpha = 0$. Furthermore, the relative transferability of MEKRR compared to the other methods even improves as the task becomes harder. It is worth noting that D_1, D_2, D_3 are qualitatively similar, being all composed of 5 layers of Fe and differing only through the sampling method used. Instead, the atomic environments contained in D_4 are different as they refer to a slab with a different number of layers. This explains the different order of magnitudes in the last two columns. Despite this, MEKRR still performs very well compared to the baselines.

5.5 Leveraging the kernel beyond supervised learning

In the previous sections we have shown how MEKRR performs very well on both supervised and transfer learning tasks. The effectiveness comes from the combination of a pre-trained feature map

Table 1: Same-dataset energy prediction. The errors are in units of meV/atom. Best performance given by **bold** number in gray cell.

Algorithm	Fe/N ₂								Cu/formate	
	D1		D2		D3		D4		RMSE	MAE
	RMSE	MAE	RMSE	MAE	RMSE	MAE	RMSE	MAE		
SchNet	0.5	0.4	4.1	3.2	5.1	3.8	6.2	4.7	6.0	4.7
GAP-SOAP	0.4	0.4	2.1	1.5	3.9	2.9	4.9	3.0	2.8	1.4
SchNet-FT	0.1	0.1	2.0	1.5	2.5	3.2	3.2	2.6	1.9	1.5
MEKRR	0.3	0.3	1.5	1.2	2.2	1.7	2.2	1.8	1.7	0.9
MEKRR- α	0.1	0.1	1.3	0.9	2.4	1.7	3.3	2.3	1.2	0.6

Table 2: Transfer evaluation of algorithms on source to target: $D_{\text{source}} \rightarrow D_{\text{target}}$. The errors are in units of meV/atom. Best performance given by **bold** number in gray cell.

Algorithm	$D_1 \rightarrow D_2$		$D_1 \rightarrow D_3$		$D_2 \rightarrow D_3$		$D_2 \rightarrow D_4$		$D_3 \rightarrow D_4$	
	RMSE	MAE	RMSE	MAE	RMSE	MAE	RMSE	MAE	RMSE	MAE
SchNet	13.2	10.1	15.4	12.3	6.2	4.9	93	90	107	105
GAP-SOAP	24.9	14.6	59.1	34.1	5.8	4.2	830	829	888	888
SchNet-FT	17.6	13.6	27.3	19.4	3.7	2.8	121	119	116	114
MEKRR	8.0	5.6	9.3	6.9	2.9	2.2	27	20	55	51

together with the K_α kernel. However, we can leverage the similarity measure provided by the kernel for tasks beyond potential energy regression. For this purpose, in Fig. 2 we plot the kernel matrix of a part of the trajectory of D_2 containing an N-N bond breaking event in the cases $\alpha = 0$ and $\alpha = 1$. In both images we can see a clear structure that highlights at least two distinct states, but with the second heatmap having more signal. We can then use the kernel to perform spectral clustering with two classes, the result is visualized on the top margin of the heatmap along with the time evolution of a physical quantity that signals the N-N bond-breaking. This facilitates a physical interpretation, as the two classes correspond to configurations containing the reactants (the N₂ molecule) and products (two N atoms) of the chemical reaction. Interestingly, the $\alpha = 1$ case correlates more closely with the handpicked physical quantity, shown in the top panel. The reason for this is the fact that learning the weights independently gives more weight to chemical species that are under-represented, which typically correspond to adsorbed atoms in surfaces. This allows us to give more weight to the most important actors in catalytic applications.

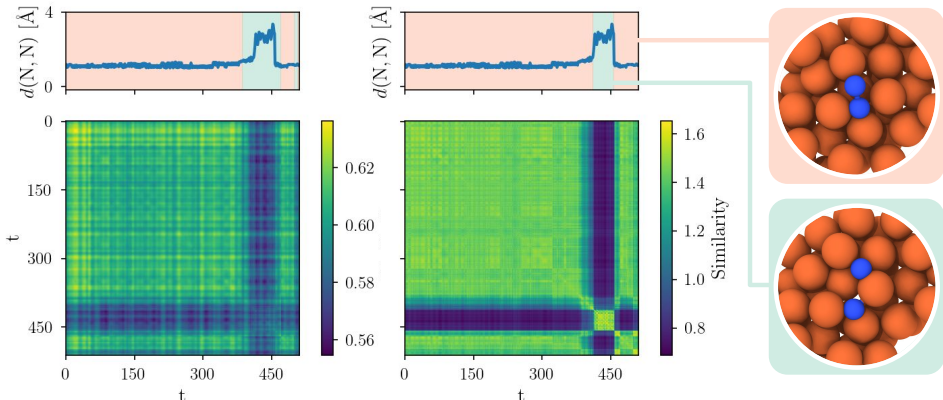


Figure 2: Heatmaps of the K_α kernel applied to a part of the trajectory of D_2 (where a reactive event occurs) and time series of the distance between nitrogen atoms over time t . The cases with $\alpha = 0$ and $\alpha = 1$ are reported on the left and right, respectively. Using spectral clustering with the two kernels as inputs we label each time-index with one of two classes, with the background color showing the class. Spectral clustering with the multi-weight kernel picks out the reactive event perfectly.

6 Conclusion and future work

In this work, we introduced an approach to model the potential energy surface of atomistic systems. This method employs pre-trained GNN representations on the large OC20 dataset and kernel ridge regression applied to downstream tasks of *ab initio* simulations of two catalytic processes out-of-distribution of the pre-training dataset. We devised a kernel function incorporating GNN features, blending kernel mean embedding with information related to the atom’s chemical species. Our approach outperforms standalone GNN or kernel methods, demonstrating impressive transferability. This suggests promising avenues for transfer learning application in computational chemistry. However, we recognize certain limitations. Our method’s scalability to larger downstream datasets is yet to be improved, and it currently does not incorporate additional data such as forces. We believe that addressing these aspects will further enhance this framework’s impact in computational chemistry.

References

- [1] Daan Frenkel and Berend Smit. *Understanding Molecular Simulation: From Algorithms to Applications*, volume 1. Elsevier, 2001.
- [2] John E. Lennard-Jones. Cohesion. *Proceedings of the Physical Society*, 43(5):461, 1931.
- [3] Richard Car and Michele Parrinello. Unified approach for molecular dynamics and density-functional theory. *Physical Review Letters*, 55(22):2471, 1985.
- [4] Dominik Marx and Jurg Hutter. Ab initio molecular dynamics: Theory and implementation. *Modern Methods and Algorithms of Quantum Chemistry*, 1(301-449):141, 2000.
- [5] Walter Kohn and Lu Jeu Sham. Self-consistent equations including exchange and correlation effects. *Physical review*, 140(4A):A1133, 1965.
- [6] Jörg Behler and Michele Parrinello. Generalized neural-network representation of high-dimensional potential-energy surfaces. *Physical Review Letters*, 98(14):146401, 2007.
- [7] Oliver T. Unke, Stefan Chmiela, Huziel E. Sauceda, Michael Gastegger, Igor Poltavsky, Kristof T. Schütt, Alexandre Tkatchenko, and Klaus-Robert Müller. Machine Learning Force Fields. *Chemical Reviews*, 121(16):10142–10186, 2021.
- [8] Jörg Behler and Gábor Csányi. Machine learning potentials for extended systems: a perspective. *The European Physical Journal B*, 94:1–11, 2021.
- [9] Albert P. Bartók, Mike C. Payne, Risi Kondor, and Gábor Csányi. Gaussian Approximation Potentials: The Accuracy of Quantum Mechanics, without the Electrons. *Physical Review Letters*, 104(13):136403, 2010.
- [10] Stefan Chmiela, Alexandre Tkatchenko, Huziel E. Sauceda, Igor Poltavsky, Kristof T. Schütt, and Klaus-Robert Müller. Machine learning of accurate energy-conserving molecular force fields. *Science Advances*, 3(5):e1603015, 2017.
- [11] Volker L. Deringer, Albert P. Bartók, Noam Bernstein, David M. Wilkins, Michele Ceriotti, and Gábor Csányi. Gaussian Process Regression for Materials and Molecules. *Chemical Reviews*, 121(16):10073–10141, 2021.
- [12] Kristof Schütt, Pieter-Jan Kindermans, Huziel Enoc Sauceda Felix, Stefan Chmiela, Alexandre Tkatchenko, and Klaus-Robert Müller. SchNet: A continuous-filter convolutional neural network for modeling quantum interactions. In *Advances in Neural Information Processing Systems*, volume 30. Curran Associates, Inc., 2017.
- [13] Johannes Klicpera, Janek Groß, and Stephan Günnemann. Directional Message Passing for Molecular Graphs. In *Eighth International Conference on Learning Representations*, 2020.
- [14] Tian Xie and Jeffrey C. Grossman. Crystal Graph Convolutional Neural Networks for an Accurate and Interpretable Prediction of Material Properties. *Physical Review Letters*, 120(14):145301, 2018.

- [15] Victor Garcia Satorras, Emiel Hooeboom, and Max Welling. E(n) Equivariant Graph Neural Networks, 2022.
- [16] Simon Batzner, Albert Musaelian, Lixin Sun, Mario Geiger, Jonathan P. Mailoa, Mordechai Kornbluth, Nicola Molinari, Tess E. Smidt, and Boris Kozinsky. E(3)-equivariant graph neural networks for data-efficient and accurate interatomic potentials. *Nature Communications*, 13(1):2453, 2022.
- [17] Linfeng Zhang, Jiequn Han, Han Wang, Wissam Saidi, Roberto Car, et al. End-to-end symmetry preserving inter-atomic potential energy model for finite and extended systems. *Advances in Neural Information Processing Systems*, 31, 2018.
- [18] Albert P. Bartók, Risi Kondor, and Gábor Csányi. On representing chemical environments. *Physical Review B*, 87(18):184115, 2013.
- [19] Michael J Willatt, Félix Musil, and Michele Ceriotti. Atom-density representations for machine learning. *The Journal of Chemical Physics*, 150(15):154110, 2019.
- [20] Felix Musil, Andrea Grisafi, Albert P Bartók, Christoph Ortner, Gábor Csányi, and Michele Ceriotti. Physics-inspired structural representations for molecules and materials. *Chemical Reviews*, 121(16):9759–9815, 2021.
- [21] Lowik Chanussot, Abhishek Das, Siddharth Goyal, Thibaut Lavril, Muhammed Shuaibi, Morgane Riviere, Kevin Tran, Javier Heras-Domingo, Caleb Ho, Weihua Hu, Aini Palizhati, Anuroop Sriram, Brandon Wood, Junwoong Yoon, Devi Parikh, C. Lawrence Zitnick, and Zachary Ulissi. The Open Catalyst 2020 (OC20) Dataset and Community Challenges. *ACS Catalysis*, 11(10):6059–6072, 2021.
- [22] Olga Russakovsky, Jia Deng, Hao Su, Jonathan Krause, Sanjeev Satheesh, Sean Ma, Zhiheng Huang, Andrej Karpathy, Aditya Khosla, Michael Bernstein, Alexander C. Berg, and Li Fei-Fei. ImageNet Large Scale Visual Recognition Challenge. *International Journal of Computer Vision*, 115(3):211–252, 2015.
- [23] Jia Deng, Wei Dong, Richard Socher, Li-Jia Li, Kai Li, and Li Fei-Fei. ImageNet: A large-scale hierarchical image database. In *2009 IEEE Conference on Computer Vision and Pattern Recognition*, pages 248–255, 2009.
- [24] Eleni Triantafyllou, Tyler Zhu, Vincent Dumoulin, Pascal Lamblin, Utku Evci, Kelvin Xu, Ross Goroshin, Carles Gelada, Kevin Swersky, Pierre-Antoine Manzagol, and Hugo Larochelle. Meta-Dataset: A Dataset of Datasets for Learning to Learn from Few Examples. In *International Conference on Learning Representations*, 2020.
- [25] Xiaohua Zhai, Joan Puigcerver, Alexander Kolesnikov, Pierre Ruysen, Carlos Riquelme, Mario Lucic, Josip Djolonga, Andre Susano Pinto, Maxim Neumann, Alexey Dosovitskiy, Lucas Beyer, Olivier Bachem, Michael Tschannen, Marcin Michalski, Olivier Bousquet, Sylvain Gelly, and Neil Houlsby. A Large-scale Study of Representation Learning with the Visual Task Adaptation Benchmark, 2020.
- [26] Ahmad Ghazal, Tilmann Rabl, Minqing Hu, Francois Raab, Meikel Poess, Alain Crolotte, and Hans-Arno Jacobsen. BigBench: Towards an industry standard benchmark for big data analytics. In *Proceedings of the 2013 ACM SIGMOD International Conference on Management of Data*, SIGMOD '13, pages 1197–1208, New York, NY, USA, 2013. Association for Computing Machinery.
- [27] Alex Wang, Yada Pruksachatkun, Nikita Nangia, Amanpreet Singh, Julian Michael, Felix Hill, Omer Levy, and Samuel Bowman. SuperGLUE: A Stickier Benchmark for General-Purpose Language Understanding Systems. In *Advances in Neural Information Processing Systems*, volume 32. Curran Associates, Inc., 2019.
- [28] Rishi Bommasani, Drew A. Hudson, Ehsan Adeli, Russ Altman, Simran Arora, Sydney von Arx, Michael S. Bernstein, Jeannette Bohg, Antoine Bosselut, Emma Brunskill, Erik Brynjolfsson, Shyamal Buch, Dallas Card, Rodrigo Castellon, Niladri Chatterji, Annie Chen, Kathleen Creel, Jared Quincy Davis, Dora Demszky, Chris Donahue, Moussa Doumbouya, Esin Durmus, Stefano

- Ermon, John Etchemendy, Kawin Ethayarajh, Li Fei-Fei, Chelsea Finn, Trevor Gale, Lauren Gillespie, Karan Goel, Noah Goodman, Shelby Grossman, Neel Guha, Tatsunori Hashimoto, Peter Henderson, John Hewitt, Daniel E. Ho, Jenny Hong, Kyle Hsu, Jing Huang, Thomas Icard, Saahil Jain, Dan Jurafsky, Pratyusha Kalluri, Siddharth Karamcheti, Geoff Keeling, Fereshthe Khani, Omar Khattab, Pang Wei Koh, Mark Krass, Ranjay Krishna, Rohith Kuditipudi, Ananya Kumar, Faisal Ladhak, Mina Lee, Tony Lee, Jure Leskovec, Isabelle Levent, Xiang Lisa Li, Xuechen Li, Tengyu Ma, Ali Malik, Christopher D. Manning, Suvir Mirchandani, Eric Mitchell, Zanele Munyikwa, Suraj Nair, Avanika Narayan, Deepak Narayanan, Ben Newman, Allen Nie, Juan Carlos Niebles, Hamed Nilforoshan, Julian Nyarko, Giray Ogut, Laurel Orr, Isabel Papadimitriou, Joon Sung Park, Chris Piech, Eva Portelance, Christopher Potts, Aditi Raghunathan, Rob Reich, Hongyu Ren, Frieda Rong, Yusuf Roohani, Camilo Ruiz, Jack Ryan, Christopher Ré, Dorsa Sadigh, Shiori Sagawa, Keshav Santhanam, Andy Shih, Krishnan Srinivasan, Alex Tamkin, Rohan Taori, Armin W. Thomas, Florian Tramèr, Rose E. Wang, William Wang, Bohan Wu, Jiajun Wu, Yuhuai Wu, Sang Michael Xie, Michihiro Yasunaga, Jiaxuan You, Matei Zaharia, Michael Zhang, Tianyi Zhang, Xikun Zhang, Yuhui Zhang, Lucia Zheng, Kaitlyn Zhou, and Percy Liang. On the Opportunities and Risks of Foundation Models, 2022.
- [29] Liam Collins, Aryan Mokhtari, Sewoong Oh, and Sanjay Shakkottai. MAML and ANIL Provably Learn Representations. In *Proceedings of the 39th International Conference on Machine Learning*, pages 4238–4310. PMLR, 2022.
- [30] John Isak Texas Falk, Carlo Cilibert, and Massimiliano Pontil. Implicit kernel meta-learning using kernel integral forms. In *Proceedings of the Thirty-Eighth Conference on Uncertainty in Artificial Intelligence*, pages 652–662. PMLR, 2022.
- [31] Guneet Singh Dhillon, Pratik Chaudhari, Avinash Ravichandran, and Stefano Soatto. A Baseline for Few-Shot Image Classification. In *International Conference on Learning Representations*, 2023.
- [32] Jake Snell, Kevin Swersky, and Richard Zemel. Prototypical Networks for Few-shot Learning. In *Advances in Neural Information Processing Systems*, volume 30, 2017.
- [33] Luca Bertinetto, Joao F. Henriques, Philip Torr, and Andrea Vedaldi. Meta-learning with differentiable closed-form solvers. In *International Conference on Learning Representations*, 2023.
- [34] Duo Zhang, Hangrui Bi, Fu-Zhi Dai, Wanrun Jiang, Linfeng Zhang, and Han Wang. Dpa-1: Pretraining of attention-based deep potential model for molecular simulation. *arXiv preprint arXiv:2208.08236*, 2022.
- [35] Stefan Chmiela, Huziel E. Sauceda, Igor Poltavsky, Klaus-Robert Müller, and Alexandre Tkatchenko. sGDML: Constructing accurate and data efficient molecular force fields using machine learning. *Computer Physics Communications*, 240:38–45, 2019.
- [36] Stefan Chmiela, Valentin Vassilev-Galindo, Oliver T. Unke, Adil Kabylda, Huziel E. Sauceda, Alexandre Tkatchenko, and Klaus-Robert Müller. Accurate global machine learning force fields for molecules with hundreds of atoms. *Science Advances*, 9(2):eadf0873, 2023.
- [37] Niklas Frederik Schmitz, Klaus-Robert Müller, and Stefan Chmiela. Algorithmic Differentiation for Automated Modeling of Machine Learned Force Fields. *The Journal of Physical Chemistry Letters*, 2022.
- [38] Kristof T. Schütt, Oliver T. Unke, and Michael Gastegger. Equivariant message passing for the prediction of tensorial properties and molecular spectra, 2021.
- [39] Bernhard Schölkopf and Alexander J. Smola. *Learning with Kernels: Support Vector Machines, Regularization, Optimization, and Beyond*. The MIT Press, 2018.
- [40] Krikamol Muandet, Kenji Fukumizu, Bharath Sriperumbudur, and Bernhard Schölkopf. Kernel Mean Embedding of Distributions: A Review and Beyond. *Foundations and Trends® in Machine Learning*, 10(1-2):1–141, 2017.

- [41] Arthur E. Hoerl and Robert W. Kennard. Ridge Regression: Biased Estimation for Nonorthogonal Problems. *Technometrics*, 12(1):55–67, 1970.
- [42] Lei Shi, Xin Guo, and Ding-Xuan Zhou. Hermite learning with gradient data. *Journal of Computational and Applied Mathematics*, 233(11):3046–3059, 2010.
- [43] Michael M. Bronstein, Joan Bruna, Taco Cohen, and Petar Veličković. Geometric Deep Learning: Grids, Groups, Graphs, Geodesics, and Gauges, 2021.
- [44] Jie Zhou, Ganqu Cui, Shengding Hu, Zhengyan Zhang, Cheng Yang, Zhiyuan Liu, Lifeng Wang, Changcheng Li, and Maosong Sun. Graph neural networks: A review of methods and applications. *AI Open*, 1:57–81, 2020.
- [45] Kristof T. Schütt, Huziel E. Sauceda, Pieter-Jan Kindermans, Alexandre Tkatchenko, and Klaus-Robert Müller. SchNet - a deep learning architecture for molecules and materials. *The Journal of Chemical Physics*, 148(24):241722, 2018.
- [46] Johannes Gasteiger, Florian Becker, and Stephan Günnemann. GemNet: Universal Directional Graph Neural Networks for Molecules, 2022.
- [47] Weihua Hu, Muhammed Shuaibi, Abhishek Das, Siddharth Goyal, Anuroop Sriram, Jure Leskovec, Devi Parikh, and C. Lawrence Zitnick. ForceNet: A Graph Neural Network for Large-Scale Quantum Calculations, 2021.
- [48] Kristof T. Schütt, Farhad Arbabzadah, Stefan Chmiela, Klaus R. Müller, and Alexandre Tkatchenko. Quantum-chemical insights from deep tensor neural networks. *Nature Communications*, 8(1):13890, 2017.
- [49] Johannes Gasteiger, Muhammed Shuaibi, Anuroop Sriram, Stephan Günnemann, Zachary Ulissi, C. Lawrence Zitnick, and Abhishek Das. GemNet-OC: Developing Graph Neural Networks for Large and Diverse Molecular Simulation Datasets, 2022.
- [50] Theodoros Evgeniou and Massimiliano Pontil. Regularized multi-task learning. In *Proceedings of the 10th ACM SIGKDD International Conference on Knowledge Discovery and Data Mining*, pages 109–117, 2004.
- [51] Theodoros Evgeniou, Charles A. Micchelli, and Massimiliano Pontil. Learning multiple tasks with kernel methods. *Journal of Machine Learning Research*, 6(21):615–637, 2005.
- [52] Kristof T. Schütt, Huziel E. Sauceda, Pieter-Jan Kindermans, Alexandre Tkatchenko, and Klaus-Robert Müller. SchNet – A deep learning architecture for molecules and materials. *The Journal of Chemical Physics*, 148(24):241722, 2018.
- [53] Albert P. Bartók, Risi Kondor, and Gábor Csányi. On representing chemical environments. *Physical Review B*, 87(18):184115, 2013.
- [54] James R. Kermode. F90wrap: An automated tool for constructing deep Python interfaces to modern Fortran codes. *Journal of Physics: Condensed Matter*, 32(30):305901, 2020.
- [55] Gabor Csanyi, Steven Winfield, James Kermode, Mike Payne, Alessio Comisso, Alessandro De Vita, and Noam Bernstein. Expressive Programming for Computational Physics in Fortran 950+. *Newsletter of the Computational Physics Group*, pages 1–24, 2007.
- [56] Damien Garreau, Wittawat Jitkrittum, and Motonobu Kanagawa. Large sample analysis of the median heuristic, 2018.
- [57] Luigi Bonati, Daniela Polino, Cristina Pizzolitto, Pierdomenico Biasi, Rene Eckert, Stephan Reitmeier, Robert Schlögl, and Michele Parrinello. Non-linear temperature dependence of nitrogen adsorption and decomposition on fe (111) surface. *Cambridge: Cambridge Open Engage*, 2023.
- [58] Alessandro Laio and Michele Parrinello. Escaping free-energy minima. *Proceedings of the national academy of sciences*, 99(20):12562–12566, 2002.

- [59] Manyi Yang, Luigi Bonati, Daniela Polino, and Michele Parrinello. Using metadynamics to build neural network potentials for reactive events: the case of urea decomposition in water. *Catalysis Today*, 387:143–149, 2022.
- [60] Tom Brown, Benjamin Mann, Nick Ryder, Melanie Subbiah, Jared D Kaplan, Prafulla Dhariwal, Arvind Neelakantan, Pranav Shyam, Girish Sastry, Amanda Askell, Sandhini Agarwal, Ariel Herbert-Voss, Gretchen Krueger, Tom Henighan, Rewon Child, Aditya Ramesh, Daniel Ziegler, Jeffrey Wu, Clemens Winter, Chris Hesse, Mark Chen, Eric Sigler, Mateusz Litwin, Scott Gray, Benjamin Chess, Jack Clark, Christopher Berner, Sam McCandlish, Alec Radford, Ilya Sutskever, and Dario Amodei. Language Models are Few-Shot Learners. In *Advances in Neural Information Processing Systems*, volume 33, pages 1877–1901, 2020.
- [61] Karl Weiss, Taghi M. Khoshgoftaar, and DingDing Wang. A survey of transfer learning. *Journal of Big Data*, 3(1):9, 2016.
- [62] Justin S. Smith, Benjamin T. Nebgen, Roman Zubatyuk, Nicholas Lubbers, Christian Devereux, Kipton Barros, Sergei Tretiak, Olexandr Isayev, and Adrian E. Roitberg. Approaching coupled cluster accuracy with a general-purpose neural network potential through transfer learning. *Nature Communications*, 10(1):2903, 2019.

Supplementary Material

This appendix is organized as follows: in Appendix A we derive the multi-weight KRR outlined in Section 4.1 in the main paper. In Appendix B we show times for training the algorithms and discuss this. In Appendix C we provide details on the algorithms and hyperparameters used in the paper, and conduct additional experiments to those in Section 5.

A Multi-weight KRR

In this section, we show that the problem of optimizing the objective function (4) over the parameters w_0, v_1, \dots, v_S is equivalent to kernel ridge regression. For the convenience of the reader we rewrite the objective function,

$$\sum_{t=1}^T \left(E_t - \sum_{s=1}^S \langle v_s + w_0, \phi(H_{t,s}) \rangle \right)^2 + \lambda \left(\frac{1}{\alpha} \sum_{s=1}^S \|v_s\|^2 + \frac{1}{1-\alpha} \|w_0\|^2 \right). \quad (6)$$

Our reasoning follows that in [50, 51] for the multi-task learning setting. Notably here, we work with embedding kernels and a different loss function, hence the final results is conceptually different.

We recall the notation of node-feature sets $H_t = (h_{t,i} | i \in [n])$ where $t \in [T]$ is the index running over training configurations. Moreover we use the notation $H_{t,s} = (h_{t,i} | z_{t,i} = s)$, where $z_{t,i} \in [S]$ denotes the chemical species of atom i in the configuration t . We also recall the feature map ϕ on sets, defined as

$$\phi(H) = C_H \sum_{i=1}^n \phi(h_i), \quad H = (h_i | i \in [n]).$$

Next we make a change of variable $u_s = \frac{v_s}{\sqrt{\alpha}}$, $s \in [S]$, and $u_0 = \frac{w_0}{\sqrt{1-\alpha}}$. Then let

$$\mathbf{u} = (u_0, u_1, \dots, u_S), \quad \text{and} \quad \Psi(H_t, z_t) = \left(\sqrt{1-\alpha} \phi(H_t), \sqrt{\alpha} \phi(H_{t,1}), \dots, \sqrt{\alpha} \phi(H_{t,S}) \right).$$

For any $\mathbf{u} = (u_0, u_1, \dots, u_S)$ and $\mathbf{u}' = (u'_0, u'_1, \dots, u'_S)$ we also define the inner product $\langle \mathbf{u}, \mathbf{u}' \rangle = \sum_{s=0}^S \langle u_s, u'_s \rangle$. With this notation at hand the objective function (6) can be rewritten as

$$\sum_{t=1}^T \left(E_t - \langle \mathbf{u}, \Psi(H_t, z_t) \rangle \right)^2 + \lambda \|\mathbf{u}\|^2$$

which we recognize as the usual KRR objective with RKHS given by the kernel in (5). Notice that this reasoning applies whenever $\alpha \in (0, 1)$. The cases $\alpha = 0$ or $\alpha = 1$ can be treated following a similar reasoning, leading to the two particular cases of KRR with kernel (5). For instance, if $\alpha = 1$, since we aim to minimize the objective (6), we can drop the variable w_0 as at the optimum $w_0 = 0$.

B Timings

Table 3: Timings (mean \pm std) in seconds for training all algorithms using the same algorithmic settings as for Table 1 for D_1, D_4 and the Cu/formate datasets. MEKRR $\alpha = 0$ is much faster than the competitors despite being the most competitive in terms of performance (as seen in Table 1). The timings were aggregated over three independent runs. For each dataset we specify the number of configurations T , atoms n and species S using a tuple (T, n, S) . Best performance given by **bold** number in gray cell.

Algorithm	D_1 (720, 47, 2)	D_4 (600, 74, 2)	Cu/formate (1000, 52, 4)
SchNet	482.7 \pm 1.7	511.9 \pm 4.5	585.4 \pm 4.3
GAP-SOAP	52.3 \pm 0.9	69.1 \pm 0.6	282.3 \pm 1.6
SchNet-FT	442.2 \pm 0.8	626.8 \pm 1.6	708.2 \pm 0.4
MEKRR	20.2 \pm 0.4	38.5 \pm 0.0	43.0 \pm 1.2

As can be seen from Table 3, MEKRR is the fastest to train by a wide margin. While train time is dependent on both the size of the problem in terms of number of configurations T , number of atoms

n and number of chemical species S and the specific hyperparameter used, this shows that for these settings, MEKRR performs well without sacrificing speed. A thing of note is that the train time of MEKRR is not drastically impacted by the number of chemical species S compared to GAP-SOAP.

C Experiments

C.1 Hardware Specification

OS Ubuntu 20.04.6 LTS

RAM 128GB

CPU AMD Ryzen Threadripper PRO 5965WX 24-Cores

GPU NVIDIA GeForce RTX 3090

C.2 Algorithm specification

We specify in more detail the algorithms and hyperparameter choices. For an exact specification, please inspect the supplied code base. All of the algorithms use periodic boundary conditions in all directions. For the same-system predictions for SchNet, SchNet-FT, and MEKRR we standardize the data, while for the transfer-system predictions, for all algorithms, we remove the mean using a precomputed dictionary $\bar{\epsilon} \in \mathbb{R}^S$ of the energies of each species s , so that the energy becomes $E \mapsto E - \sum_i^n \bar{\epsilon}_{z_i}$ and at test time we predict this residual and add back the correct sum.

SchNet We use the implementation of the [OCP20 code base](#) with the number of hidden channels being 256, number of filters being 64, number of interactions being 3 and number of Gaussians in the basis expansion being 200 and a cutoff for generating the graphs being 6.0Å. We perform optimization using the MSE objective with no regularization and use the AdamW optimizer with the amsgrad option and no weight decay with a learning rate of 10^{-4} . We use a batch size of 16 and optimize for 800 epochs, saving the weights with the best validation error on the validation set using RMSE as the validation objective.

GAP-SOAP As specified in the main body, we use the quippy python interface of the QUIP implementation of GAP. We set the following parameters in the command line interface `gap_fit` where we use the soap parameters `atom_sigma = 0.5, l_max = 6, n_max = 12, cutoff = 6.0, cutoff_transition_width = 1.0, delta = 0.2, covariance_type = dot_product, n_sparse = 1000, zeta = 4, energy_scale = 1.0, atom_gaussian_width = 1.0` and additional parameters of `default_sigma = [0.001, 0., 0.0, 0.0], e0_method = average`, except for the transfer learning experiments where we instead remove the average using precomputed atom-specific energies as specified in the top paragraph of this section.

SchNet-FT We use the implementation of the [OCP20 code base](#) where we use the pretrained weights of https://dl.fbaipublicfiles.com/opencatalystproject/models/2020_11/s2ef/schnet_all_large.pt and config <https://github.com/Open-Catalyst-Project/ocp/blob/main/configs/s2ef/all/schnet/schnet.yml> (SchNet, trained on the split All in the [OCP20 models table](#)). This model has the hyperparameters of number of hidden channels being 1024, the number of filters being 256, the number of interactions being 5, number of Gaussians in the basis expansion being 200 and a cutoff for generating the graphs being 6.0Å. We freeze layers up to layer 3. We fit the remaining parameters by optimization using the MSE objective with no regularization and use the AdamW optimizer with the amsgrad option and no weight decay with a learning rate of 10^{-4} . We use a batch size of 16 and optimize for 200 epochs, saving the weights with the best validation error on the validation set using RMSE as the validation objective.

MEKRR- α For the representation we use the same pretrained weights and configuration as those of SchNet-FT above, and for representation we use the output of the second layer. For the datasets in Table 1 we use $\lambda = 10^{-7}$ and $\alpha = 1.0, 10^{-2}$ for the Fe/N₂ and Cu/Formate datasets, respectively with $C = 1/n$. For the datasets in Table 2 we use $\lambda = 10^{-4}$ and $\alpha = 0.0$.

In order to transfer between different system sizes (as in Table 2) we note that, if the model has been trained with data $(H_t)_{t=1}^T$ from a system of given size, and one wants to estimate the energy $E(H)$

of a configuration H belonging to a system of different size n_H whose node embeddings are $(h_i)_{i=1}^{n_H}$, one has

$$E(H) \approx f(H) = \sum_{i=1}^{n_H} \sum_{t=1}^T c_t \langle \phi(h_i), \phi(H_t) \rangle$$

where $(c_t)_{t=1}^T$ are the fitted coefficients for MEKRR. For this reason, in this setting we use C equal to 1.

C.3 Additional experiments

Necessity of non-linear kernel in MEKRR To show that averaging the node-features from the pretrained SchNet GNN fails to learn we apply MEKRR with a linear kernel to the output of the second layer to the pretrained SchNet. The results are shown in Table 4. We can clearly see that Linear-KRR (MEKRR with a linear kernel applied to SchNet) fails to perform well highlighting the need for a non-linear kernel for MEKRR to work.

Table 4: Comparison between linear and Gaussian kernel, same-dataset energy prediction for the Fe/N₂ datasets D_i . The errors are in units of meV/atom. Best performance given by **bold** number in gray cell.

Algorithm	$D1$		$D2$		$D3$		$D4$	
	RMSE	MAE	RMSE	MAE	RMSE	MAE	RMSE	MAE
Linear-KRR	72	69	198	166	66	53	146	118
Linear-KRR- $(\alpha = 1)$	21	18	155	125	161	128	55	40
MEKRR	0.3	0.3	1.5	1.2	2.2	1.7	2.2	1.8
MEKRR- $(\alpha = 1)$	0.1	0.1	1.3	0.9	2.4	1.7	3.3	2.3

Representation layer In all experiments we construct the feature vector of the MEKRR method as the output of the second layer of the SchNet pre-trained model. This is motivated by the tradeoff between memory, computation and performance. In this section we report the results when varying the number of layers for performance on the same-energy prediction on dataset D_2 (Table 5), showing a slight increase in performances. Furthermore, we report the visualizations of the kernel matrix in Fig. 3. For both tasks, we observe an improvement when using the MEKRR- α variant.

Table 5: Comparison of MEKRR using different representation layers for the feature map, tested on the same-dataset energy prediction task for the Fe/N₂ dataset D_2 . The errors are in units of meV/atom.

Layer	$\alpha = 0$		$\alpha = 1$	
	RMSE	MAE	RMSE	MAE
1	1.9	1.4	1.7	1.2
2	1.5	1.1	1.3	0.9
3	1.4	1.0	1.0	0.7
4	1.4	1.0	1.0	0.7
5	1.4	1.0	0.9	0.6

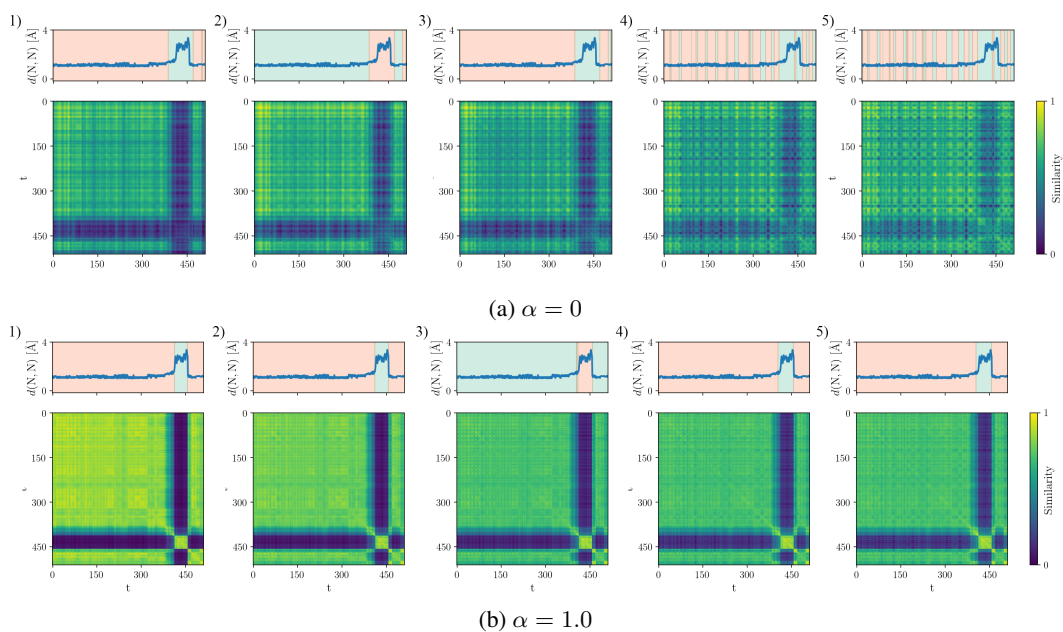


Figure 3: Heatmaps of the K_α kernel applied when k is Gaussian (lengthscale fit with median heuristic) and the node-features are given by the L 'th layer $L = 1, \dots, 5$ of the pretrained SchNet GNN going from the leftmost to rightmost column, to a part of the trajectory of D_2 (where a reactive event occurs) and time series of the distance between nitrogen atoms over time t . The cases with $\alpha = 0$ and $\alpha = 1$ are reported above and below, respectively. Using spectral clustering with the two kernels as inputs we label each time-index with one of two classes, with the background color showing the class. The color has been normalized to be between 0 and 1 which does not affect the clustering or visualization. We can see that output representation from later layers yield more patterned kernel matrices with more erratic clustering. Using the multi-weight kernel K_α where $\alpha = 1$ gives better results across the board.